Air stagnation in Europe: spatiotemporal variability and impact on air quality

Jose M. Garrido-Perez[1,2], Carlos Ordóñez[1], Ricardo García-Herrera[1,2], David Barriopedro[2]

[1]Departmento de Física de la Tierra y Astrofísica, Facultad de Ciencias Físicas, Universidad Complutense de Madrid, Madrid, 28040, Spain

[2]Instituto de Geociencias (IGEO, CSIC-UCM), C. Doctor Severo Ochoa, 7, Madrid, 28040, Spain

Abstract. This paper characterizes the spatiotemporal variability of air stagnation over the Euro-Mediterranean area for the 1979-2016 period by using a simplified air stagnation index (ASI) based on daily precipitation as well as near-surface and upper wind speed data. We have also undertaken the first comparison of stagnation as derived from meteorological reanalysis and observations, finding a reasonably good agreement between both datasets. The main differences arise from the surface wind speed, as this field depends on the local setting of the observational sites and imperfect parameterizations within the reanalysis model. Since air stagnation has considerable spatial heterogeneity over the region, we have regionalized the monthly frequency of stagnant days, resulting five regions with consistent temporal patterns: Scandinavia (SCAN), Northern-Europe (NEU), Central-Europe (CEU), South-West (SW) and South-East (SE). The northern regions (SCAN and NEU), which are affected by moderately strong near-surface winds and ample precipitation, present low frequency and temporal variability in stagnation compared to the southern regions (SW and SE). The winters and summers with the highest stagnation frequency often concur with positive 500 hPa geopotential height anomalies over the regions, with the exception of negative anomalies and a displacement of the extratropical jet to the south in the case of SCAN and NEU during winter. Air stagnation exerts a clear influence on air quality (AQ), with anomalies above 10% for summer ozone (O_3) and 30% for winter PM_{10} (particulate matter ≤ 10 μm in diameter) on stagnant vs. non-stagnant days over most of the regions. These values exceed 20% and 50%, respectively, in the case of CEU, where air stagnation also drives significant changes in the frequency distributions of these pollutants and increases the likelihood of AQ exceedances. Moreover, persistent and widespread stagnation events favour the build-up of both O_3 and PM_{10} over most of the continent.

Keywords: ozone, particulate matter, air pollution, regional air quality, air stagnation, meteorology.

1 Introduction

Air stagnation situations are characterized by stable weather, weak winds in the lower to mid-troposphere and absence of precipitation. These conditions impede the horizontal dispersion and vertical mixing of air masses in the lower troposphere as well as the washout of pollutants, favouring the occurrence of poor air quality (AQ) and low visibility events (e.g. Leibensperger et al., 2008; Tai et al., 2010; Dawson et al., 2014; Wang et al., 2016, 2017; Schnell and Prather, 2017). Therefore, air stagnation has evident socioeconomic, environmental and health impacts.

Air stagnation events are often identified by using predefined thresholds for daily averaged meteorological fields, mainly the upper- and near-surface level wind speed and precipitation (e.g. Korshover and Angell, 1982; Wang and Angell, 1999; Horton et al., 2012, 2014). Some analyses have also considered other fields such as the vertical temperature gradient within the planetary boundary layer (PBL) or the PBL height (Wang and Angell, 1999; Wang et al., 2016, 2017). The fact that the existing air stagnation indices (ASIs) are empirical often makes it necessary to adapt them to specific geographical regions, seasons or even impacts (e.g. Dawson et al., 2014; Wang et al., 2016, 2017; Huang et al., 2017).

Wang and Angell (1999) considered that there is stagnation if three conditions are simultaneously met for at least four days: sea level geostrophic wind speed < 8 m s^{-1}, 500-hPa wind speed < 13 m s^{-1} and no precipitation. The US National Oceanic and Atmospheric Administration (NOAA) National Climatic Data Center (NCDC) uses this ASI to monitor the meteorological situations which potentially favour the accumulation of air pollutants (https://www.ncdc.noaa.gov/societal-impacts/air-stagnation/overview). This index is an objective measure of synoptic-scale stagnation over the US, but the dependence of the geostrophic wind on the latitude might limit its application to other regions of the globe. Note that Wang and Angell (1999) showed that the ratio between the sea level geostrophic wind speed and the 10 m wind speed is on average around 2.5 and is not geographically dependent over the US. Therefore, the 8 m s^{-1} sea level geostrophic wind condition is approximately equivalent to a 3.2 m s^{-1} threshold for wind speed at 10 m.

Following the analyses of Wang and Angel (1999), Horton et al. (2012, 2014) introduced a simplified ASI, where the 10 m wind speed is used with a threshold of 3.2 m s^{-1}. It should be borne in mind that this field is strongly influenced by complex local conditions at the Earth's surface (e.g. orography, surface roughness). Due to the sparsity of wind speed observations, most studies have used output from meteorological reanalyses and climate models, where this variable is generated from imperfect parameterizations of the boundary layer physics. In fact, Vautard et al. (2010) showed that observed surface wind speeds have declined over continental areas of

the northern mid-latitudes, while meteorological reanalysis datasets do not exhibit such trend. This could advise against the use of reanalysis data for the characterization of air stagnation. To the authors' knowledge, the only study that has calculated this index based on observations over a large area is that by Huang et al. (2017) for China, but the consistency between ASIs derived from reanalysis and observations has not been assessed so far.

Previous studies on air stagnation and its impacts have either been conducted on global and hemispheric scales with a focus on future and past changes (Horton et al., 2012, 2014; Wang et al., 2017), or have been confined to the US (Wang and Angell, 1999; Leibensperger et al., 2008; Tai et al., 2010; Schnell and Prather, 2017; Sun et al., 2017; Xu et al., 2017), China (Wang et al., 2016; Huang et al., 2017) and specific regions in Europe (Caserini et al., 2017). As an illustration, it has been shown that the low frequency of summertime mid-latitude cyclones and frontal passages are strong predictors of stagnation and air pollution in the US (Leibensperger et al., 2008; Tai et al., 2010). Schnell and Prather (2017) analysed the co-occurrence of air stagnation with surface ozone (O_3), particulate matter (PM) and temperature over the eastern US, while Sun et al. (2017) demonstrated that the impact of stagnation on ozone is stronger than that of temperature over some regions of the US. Xu et al. (2017) used an ASI together with other meteorological variables to evaluate the variability of surface ozone over the US and its dependence on El Niño-Southern Oscillation (ENSO). Huang et al. (2017) conducted a comprehensive investigation of the spatiotemporal patterns of air stagnation in China for a 30 year period. More complex meteorological indices considering the PBL height (Wang et al., 2016, 2017) or the thermal structure of the atmosphere (Cai et al., 2017; Zou et al., 2017; Huang et al., 2018) have also been shown to reflect the conditions conducive to PM episodes in China, but most studies available in the literature have used the NCDC ASI or the adaptation by Horton et al. (2012). In particular, some results from applying the latter to global climate model simulations indicate that the Euro-Mediterranean region is one of the areas most affected by air stagnation, and that Mediterranean Europe is expected to suffer a significant increase in stagnation frequency and persistence by the late 21st century if the emissions of greenhouse gases are not reduced (Horton et al., 2014). Nonetheless, a systematic analysis of air stagnation has not been carried out for Europe and the applicability of that index to AQ studies has not been demonstrated for that region yet.

The main objectives of this paper are (i) to assess the degree of consistency between the climatological features of air stagnation as derived from a meteorological reanalysis and observations; (ii) to characterize the spatiotemporal variability of stagnation over the Euro-Mediterranean area and the triggering synoptic patterns,

and (iii) to examine the impact on the airborne concentrations of two of the main pollutants linked to serious health impacts, PM_{10} (particulate matter with aerodynamic diameter ≤ 10 μm) and O_3.

The paper is structured as follows. Section 2 introduces the meteorological and AQ data. Section 3 presents the climatology of stagnation days, events (defined as the sequence of one or more consecutive stagnation days) and their duration. These are compared for a meteorological reanalysis and observational datasets. Section 4 presents a regionalization of stagnation over Europe and investigates its temporal variability. Section 5 identifies the synoptic patterns leading to seasonal stagnation extremes in the different regions. Section 6 addresses the impact of air stagnation on AQ, with a focus on PM_{10} and O_3. Finally, the main findings are summarized in Sect. 7.

2 Data and methods

As mentioned previously, air stagnation is often defined by three meteorological variables: upper-air wind speed, near-surface wind speed and precipitation. In this work we have used the NCDC ASI adaptation by Horton et al. (2012). A day is considered as stagnant for a given location when three conditions are fulfilled simultaneously: daily mean wind speed at 10 m is lower than 3.2 m s^{-1}, 500 hPa wind speed is below 13.0 m s^{-1} and daily total precipitation is under 1.0 mm (i.e. a dry day). For each location, this yields a time series filled with ones (stagnation day) and zeros (no stagnation), which can be aggregated into monthly frequencies of stagnation days. Unlike the previous index by Wang and Angell (1999), the ASI adaptation by Horton et al. (2012) places no length requirements on stagnation events and considers them as any sequence of consecutive days meeting the previous conditions, without any minimum threshold for duration. This is appropriate for our region of study due to the presence of some areas where stagnation frequency and average duration are relatively low, as will be shown later.

Despite the existence of more complex meteorological indices which can better represent the conditions favourable to the occurrence of PM episodes over some regions (Huang et al., 2018, and references therein), the choice of a simplified index like the one used in this work is motivated by the following reasons. First, it minimizes the potential discrepancies between reanalysis and observations by reducing the number of variables that strongly depend on the model physics (e.g. PBL). Second, this index has widely been employed in the literature, being a good indicator of AQ episodes related to both PM and O_3 in other regions of the world. Hence, in principle it allows us to evaluate simultaneously the impact on pollutants affected by different meteorological mechanisms. Furthermore, previous analyses using this index have projected future increases in air stagnation over the north of the Mediterranean (Horton et al., 2014), but the ability of the index to reflect the weather conditions triggering poor AQ in the region needs to be investigated. Air stagnation will be analysed for the whole year, while the assessment of its impacts on AQ will be restricted to the seasons with the highest concentrations of those pollutants.

2.1 Meteorological data

There is no observational database providing daily precipitation, upper-air wind speed and surface wind speed simultaneously for Europe. Therefore we have used three different databases covering the period 1979-2016. Daily precipitation was obtained from the E-OBS gridded dataset (Haylock et al., 2008) at 0.25° x 0.25° horizontal resolution, which is provided by the European Climate Assessment and Dataset (ECAD) (http://www.ecad.eu/download/ensembles/download.php) (last access: March 2018).

Upper-air wind data were obtained from the Integrated Global Radiosonde Archive (IGRA) (Durre et al., 2006) (https://www.ncdc.noaa.gov/data-access/weather-balloon/integrated-global-radiosonde-archive) (last access: March 2018) provided by the NOAA's National Centers for Environmental Information (NCEI). This dataset has been tested by the data provider through a comprehensive set of quality control procedures to remove gross errors. We have only used the standard level of 500 hPa and averaged all the available measurements within a single day (often two soundings) to calculate daily average wind speed at 500 hPa for each location.

Daily average wind speed observations at 10 m above ground were obtained from the Integrated Surface Database (ISD) (Smith et al., 2011) (https://www.ncdc.noaa.gov/isd/data-access) (last access: March 2018) which is provided by the NCDC's Climate Services Branch (CSB). The data supplier controls the quality of the dataset by means of algorithms that check format, extreme values and limits, consistency between parameters and continuity between observations.

Despite the fact that some IGRA radiosondes also include 10 m wind speed data, we opted to use the ISD database. The reason lies in the greater amount of these data available in the latter. This allows averaging 10 m wind speed from a number of ISD stations located within 50 km around each IGRA's radiosonde location, in a similar way as Vautard et al. (2010). This way local effects that affect surface wind speed are smoothed. The radiosonde site is eliminated from the study if no ISD stations can be found in the proximities. We have finally used 91 IGRA sites distributed homogeneously throughout the area of study as well as 583 ISD stations (Supplementary Figure S1). The number of ISD sites used for each IGRA location is irregular, ranging from only 1 to 24. Previous studies have used simultaneously the IGRA and ISD databases both for wind (e.g. Gatey et al., 2011) and for other variables such as humidity or cloud cover data (e.g. Nygard et al., 2014). Finally, daily precipitation is taken from the closest grid of the E-OBS dataset in relation to the IGRA's radiosonde location. These two datasets have previously been used simultaneously for the evaluation of the meteorological performance of coupled chemistry-meteorology simulations over Europe and the US (Brunner et al., 2015). Thus, the joint use of three different datasets should not have a significant impact on our results.

152

153 **2.2 Meteorological reanalysis**

154 10 m and 500 hPa daily wind fields and daily precipitation from the European Centre for Medium-Range Weather
155 Forecasts (ECMWF) ERA-Interim reanalysis (Dee et al., 2011), at 0.75° x 0.75° horizontal resolution, during the
156 1979-2016 period, are used. Daily mean sea level pressure (SLP) and 500 hPa geopotential height (Z500) have
157 also been employed to characterize the synoptic patterns ruling the occurrence of seasonal extremes in air
158 stagnation. Daily precipitation has been calculated as the sum of 12-hour accumulated precipitation forecast for
159 two time intervals, from 00:00 to 12:00 and from 12:00 to 24:00 on each day. Daily averages of wind speed and
160 any other meteorological variables are calculated by averaging four analysis values at 00:00, 06:00, 12:00 and
161 18:00 for each day. Additional analyses performed for the NCEP/NCAR reanalysis (Kalnay et al., 1996), not
162 shown, indicate that the results presented in this work are not very sensitive to the choice of the reanalysis
163 dataset.

164

165 **2.3 Air quality observations**

166 The impact of air stagnation on AQ is quantified in this study through two of the most relevant pollutants in
167 Europe: PM_{10} and O_3. The analyses are separately done for the two seasons with the highest concentrations of
168 these pollutants over large parts of the continent: winter (December-January-February, DJF) for PM_{10} and
169 summer (June-July-August, JJA) for O_3 (e.g. Laurila, 1999; Koelemeijer et al., 2006; Schnell et al., 2015;
170 Garrido-Perez et al., 2017).

171 Daily average PM_{10} concentrations for a 9 year period (December 2002 – February 2011) have been obtained
172 from two databases: the European Environment Agency's air quality database (AirBase)
173 (http://www.eea.europa.eu/data-and-maps/data/airbase-the-european-air-quality-database-8, last access:
174 March 2018) and the European Monitoring and Evaluation Programme (EMEP) (Tørseth et al., 2012)
175 (http://ebas.nilu.no/, last access: March 2018). Only stations with at least 75% of the winter data available for
176 the period of analysis have been used. This way we have selected a total of 535 sites (24 from EMEP and 511
177 from AirBase). Note that the EMEP network includes additional sites which have not been considered here
178 because they are also part of AirBase. Considering the types of measurement sites, the selected locations can
179 be classified as follows: 68.6% are background, 23.0% traffic and 8.4% industrial sites. Note that we have also
180 examined the availability of $PM_{2.5}$ (particulate matter with aerodynamic diameter ≤ 2.5 μm) observations from
181 AirBase and EMEP but finally opted for PM_{10} as it presents much better temporal and spatial coverage.

We have used an interpolated dataset of observed maximum daily 8-h running average near-surface ozone (MDA8 O_3) volume mixing ratios over Europe for the period 1998-2012 at 1° x 1° resolution (Schnell et al., 2015). This gridded dataset has been generated by blending observations from EMEP and AirBase, excluding sites of traffic type. It was initially delivered to evaluate chemical transport models (CTMs) and chemistry-climate models (CCMs) (Schnell et al., 2014, 2015). Other studies have also used it to identify the main synoptic and meteorological drivers of extreme ozone concentrations over Europe (Otero et al., 2016; Carro-Calvo et al., 2017) and to assess the impact of large scale anticyclonic patterns on O_3 (Ordóñez et al., 2017).

2.4 Clustering of air stagnation

A regionalization of air stagnation has been made by means of the k-means iterative optimization process. This technique is based on the Voronoi partition (Aurenhammer, 1991) and has been widely used to generate spatial divisions of meteorological and air quality fields (e.g. Bador et al., 2015; Carvalho et al., 2016; Lyapina et al., 2016; Carro-Calvo et al., 2017). It allows the generation of data clusters from a multidimensional dataset. In this case, we have used the time series of the number of stagnant days per month in each grid cell of the reanalysis dataset over the area of study, from which the algorithm generates a predefined number of k regions (clusters).

2.5 Characterization of the eddy-driven jet

The latitudinal position of the extratropical jet has been studied to better explain the effects of the synoptic patterns associated with stagnation. To do so, we have catalogued each day by using the daily jet latitudinal index of Woollings et al. (2010). The algorithm zonally averages the low-pass filtered, lower-tropospheric (925-700 hPa) daily mean zonal wind in the longitudes ranging from 0° to 60° W. The latitude where the zonal wind reaches its maximum is assigned to one of the latitudinal ranges corresponding to the modal positions of the jet over the Atlantic: southern (15°-44° N), central (44°-53° N) and northern (53°-75° N). The meteorological dataset used to identify the jet position is the NCEP/NCAR reanalysis with a spatial resolution of 2.5°. This resolution is sufficient, taking into account the large area considered to identify the position of the jet.

3 Annual occurrence of air stagnation in observations and reanalysis

We have first examined the ability of the reanalysis to reproduce the observed air stagnation climatology by comparing a series of benchmarks: annual frequency of stagnation days, number of events and their duration. For simplicity, in these comparisons each of the 91 locations with observations is matched to the closest

reanalysis grid cell. We are aware that more complex spatial verification methods are available in the literature, but the improvement that they bring is more relevant for cases that require higher resolution than ours (Brown et al., 2012).

Figure 1 shows the annually averaged percentage of air stagnation days (%, left), the average number of events per year (middle) and the average event duration (number of days, right). Generally, the spatial distribution of the calculated values compares relatively well between reanalysis and observations. Considering the whole dataset of 91 observational sites, we obtain a Pearson correlation coefficient (R) over 0.70 (p-value < 0.01) for both stagnation days and events, although only slightly above 0.55 for the average event duration. Mean biases (MB) for stagnation days and events are relatively low in the reanalysis compared to the observations (-1.4 % and 2.1 events respectively), with root mean squared errors (RMSE) close to 7 % for the stagnation days and 7 in the case of the events. These values are lower for the mean event duration, with zero bias and RMSE = 0.4 days. There are, however, some locations where the differences in the frequency of stagnation days between reanalysis and observations (Fig. 1, left) are high enough to indicate that further analyses are needed. In order to investigate this, we have done some additional comparisons for the three meteorological variables included in the ASI calculation.

Figure 2 displays the percentage of days that stagnation conditions are met separately for each component used in the ASI definition: precipitation below 1 mm (i.e. dry day, DD), 10 m wind speed below 3.2 m s^{-1} (W_{10}) and 500 hPa wind speed below 13 m s^{-1} (W_{500}). The comparison of reanalysis with observations for precipitation (Fig. 2, left) and upper air wind speed (Fig. 2, right) shows consistent patterns between both datasets, with R values of 0.95 and 0.93 respectively. The magnitude of the mean bias and RMSE is smaller for the upper-air wind speed than for precipitation, whose occurrence is overestimated by the reanalysis leading to reduced stagnation (MB = -7.2%). The main discrepancies between reanalysis and observations arise from the 10 m wind speed, for which R = 0.64 and RMSE = ~18%. This can be explained by the strong influence of orography together with the insufficient horizontal resolution and imperfect boundary layer parameterizations of the reanalysis model, as well as the impact of the local settings on observations. Furthermore, there are a considerable number of coastal sites, which could yield higher observed wind speeds compared to those in the reanalysis over some regions. In spite of this, the reanalysis underestimates the overall number of days fulfilling the 10 m wind condition for air stagnation (MB=-3.6 %). In conclusion, keeping in mind the reasonably fair agreement between the regional patterns of air stagnation in reanalysis and observations (Fig. 1, left), and that the main differences emerging from surface winds are highly local, it seems reasonable to use the reanalysis to

241 analyse regional-scale variability of air stagnation. In the following, we will focus on the analysis of air stagnation
242 as obtained from the reanalysis dataset, unless otherwise stated. Based on such data, the remaining part of
243 this section will describe the overall spatial patterns of air stagnation over the area of study.
244 Similarly as found by Horton et al. (2012) for the whole globe and Huang et al. (2017) for China, annual air
245 stagnation days are distributed with considerable regional heterogeneity across Europe. The highest stagnation
246 centres are located over southern Europe and northern Africa, where the stagnant conditions are met more than
247 40 % of the days over some locations (Fig. 1, left). Coastal areas show less stagnation than continental areas,
248 as can be expected due to the land-sea contrast and the overall minor presence of topographic barriers
249 compared to inland locations, which results in increased wind speed and therefore reduced air stagnation. The
250 spatial distribution of air stagnation events resembles that of stagnation days (Fig. 1, middle), with ~50 events
251 per year over large areas in the proximity of the Mediterranean and Black Seas, above 40 events in Scandinavia
252 and considerably fewer events in the British Isles, the North European Plain and the Baltic countries. Stagnation
253 events tend to be longer in areas with more stagnation days (Fig. 1, right). Their average length reaches 5 days
254 in some areas of Morocco and around 3 days north of the Mediterranean, and decreases to around 2 days or
255 less further north.
256 As expected, the spatial distribution of the percentage of days that fulfil the 10 m wind speed condition for air
257 stagnation shows substantial regional heterogeneity (Fig. 2, middle). This is the ASI component showing the
258 most similar spatial pattern to that of the frequency of air stagnation (Fig. 1, left), with a correlation coefficient of
259 0.95, although the occurrence of dry days may be more relevant to explain the north-south gradient in stagnation
260 (Fig. 2, left). As latitude decreases, so does the occurrence of precipitation and therefore the number of dry
261 days increases. The upper-air wind speed presents considerable spatial homogeneity, fulfilling the stagnation
262 condition in a range between 40 and 60% of the days for most of the study area. These values are considerably
263 low compared to those found for the other two fields over specific regions, in particular for the southern half of
264 the domain. Accordingly, upper-air wind speed may be the main limiting factor in the occurrence of stagnation
265 over some regions of southern Europe, while precipitation and 10 m wind speed would restrict it in Scandinavia
266 and the regions around the North European Plain, respectively. A more detailed regional assessment is
267 presented in the next section.

4 Spatiotemporal variability of air stagnation

4.1 Regionalization of air stagnation

We have applied the k-means clustering technique on the gridded monthly frequency of stagnation days over Europe for 1979-2016 obtained from reanalysis data. The stagnation dataset consists of a matrix filled with the number of stagnant days per month in each grid cell of the reanalysis, considering only the continental areas within the range 33° N – 75° N and 12° W – 26.25° E. This covers a region smaller than that shown in Fig. 1, as we have preferred to limit the analyses to regions with reasonably good coverage of PM_{10} and O_3 observations. The algorithm allows obtaining regions or clusters where air stagnation presents consistent temporal patterns. After some testing, we have set the number of seeds (i.e. initial cluster centres) to 30 and the maximum number of iterations to 300; these choices ensure repeatability and reproducibility of the clustering results. This has resulted in a spatial division of five regions as displayed on Fig. 3. The choice of the final number of clusters has been made as a reasonable compromise between the spatial extension and the representativeness of the regions.

From north to south and from west to east, the clusters roughly cover Scandinavia (SCAN), Northern Europe (NEU), Central Europe (CEU), the South West (SW) and South East (SE) of the domain. In general, these regions seem to be consistent with the spatial distribution of air stagnation frequency shown in Fig. 1 (left). SW (Iberian Peninsula and northern Africa) and SE (Italy and Balkans) cover a large part of the Mediterranean region, where stagnation is most frequent. NEU is basically made up by the British Isles, Benelux, Denmark and the Baltic countries, the area with the minimum frequency of stagnation. Overall, SCAN corresponds to the geographical location of the Scandinavian Peninsula, where air stagnation frequency is moderate. This is also the case for CEU, which is mainly located inside continental Europe. Note that some grid cells belonging to NEU (dark blue) and CEU (orange) are farther from their respective centroids than from others with more stagnation. This occurs because most of these cells are located close to the sea, where surface wind speed tends to be high, limiting the occurrence of stagnation compared to the surrounding regions.

4.2 Temporal variability of air stagnation

Once we have regionalized the area of study, we will first compare the seasonal cycles in each region as obtained separately from the reanalysis and the observations. This will provide further insights into the consistency between the regional features derived from reanalysis and from the embedded observational sites. In addition, we will examine the long-term variability of air stagnation in each region.

298

299 **4.2.1 Seasonal cycle**

300 Figure 4 shows the seasonal cycles of the number of stagnant days for each cluster, considering the
301 observations (red), the reanalysis grid cells closest to observational sites (blue) and the cluster centroids which
302 include all reanalysis grid cells (green) within these regions. The intervals defined by one standard deviation
303 from the mean overlap when only grid cells around the observational sites are considered (red and blue),
304 confirming a reasonably good agreement between reanalysis and observations. The largest discrepancy is
305 found for the SW region in summer, where the differences in the mean values are up to 3 days per month.
306 Moreover, if we consider every reanalysis grid cell within the cluster (green), the number of days with stagnation
307 increases considerably in that region. This result strongly suggests that the 10 observational stations available
308 for SW do not represent the behaviour of air stagnation in this cluster. Many of these stations are located in
309 coastal areas as can be seen in Fig. 1, which can explain the reduced stagnation when only those locations are
310 considered. The discrepancies when the nearest grid cells in the reanalysis are used (red and blue) may partly
311 occur because such cells cover land and sea areas, but they are also related to the biases reported previously
312 for the three components of the ASI in reanalysis and observations. The rest of clusters seem to include
313 representative enough stations, although the number of sites per region varies substantially, from only 8 in
314 SCAN to 25 in NEU. Due to these limitations in the number and representativeness of the observational sites,
315 the cluster centroid (i.e. the average monthly frequency of stagnant days for all grid cells within the region) will
316 be used for the regional analysis of the temporal variability of stagnation in the reminder part of this section.
317 Seasonal and annual series of stagnation frequency will be derived for each region by adding up the monthly
318 frequencies of the corresponding period.

319 All the reanalysis seasonal cycles (green) are characterized by a common maximum around summer (often in
320 August). Nevertheless, the month with minimum air stagnation is clearly dependent on the region, as it varies
321 from October (SCAN) to June (CEU). The largest amplitude (defined as the difference between the maximum
322 and the minimum) is found for SW and SE, with about 9 and 7 days, while it is below 4 days for the rest of the
323 clusters. This is due to the strong seasonality of both precipitation and wind in these regions.

324

325 **4.2.2 Interannual variability**

326 The interannual variability differs for the five regions. The monthly standard deviations in Fig. 4 (green bars)
327 evidence SW and SE as the regions with the largest interannual variability. The seasons when interannual

variability reaches its maximum are also different depending on the region: summer for the southern regions (SW and SE) and winter for SCAN.

To better understand the influence of the three components of the ASI in the interannual variability, we have evaluated which of them controls the temporal patterns of air stagnation over each region. For this purpose, we have computed the correlation coefficients between the regional series of stagnant days and those resulting from each component separately. Table 1 shows the individual air stagnation component that presents the highest correlation on a seasonal and yearly basis.

The table indicates that no ASI component controls uniformly the interannual variability of stagnant days in Europe, but it depends on the considered latitude. To a large extent, W_{500} drives the interannual variability of stagnation in southern Europe (SW and SE), while DD is more relevant in central regions (CEU and NEU) and W_{10} over the northernmost part of Europe (SCAN). The main driver of interannual variability does not seem to be seasonally dependent in the south of the continent, since W_{500} is selected in all seasons (with $R > 0.90$) for SW and 3 out of 4 seasons in SE. This latter region and CEU share W_{500} and DD as the main drivers of interannual variability. DD is also the dominant driver in NEU, in particular during spring-summer, while W_{10} controls the interannual variability during autumn-winter there and, during most seasons, in SCAN. Note that, while these are the general patterns, in some cases the correlation coefficients are not too different for the three ASI components. As an example, W_{500} has not been selected as the main driver of interannual variability in any season over SCAN but yields high correlations all year round, which results in this variable being selected (together with W_{10}) as the main driver of variability on an annual basis. We also stress that, with the exception of the southern regions, the main drivers of interannual variability do not necessarily correspond to the major limiting factors to the climatological occurrence of stagnant days (Fig. 2).

Finally, in order to understand the interannual variability of air stagnation at different time scales, all regions have also been tested for significant periodicities by means of a wavelet analysis (Torrence et al., 1998) applied to the time series of monthly air stagnation days. The wavelet power spectra has not revealed significant periodicities, apart from the expected presence of the annual cycle for all regions as well as a significant peak centred in the 6-8 years band for CEU (not shown), whose causes are unknown.

4.2.3 Long-term trends

Linear trends in the yearly and seasonal number of air stagnation days have been calculated for the 1979-2016 period by using ordinary least squares regression. The results are summarized in Table 2. A large area spanning

NEU, CEU and SE has undergone an upward annual trend (statistically significant at the 90% only for the first region), while weak trends are found for SCAN and SW. These trends are seasonally dependent. Over CEU there is a large (although not significant) annual trend of 2.38 days decade^{-1}, with the largest contribution in spring (1.28 days decade^{-1}). In the case of NEU, the annual increase (1.48 days decade^{-1}) is distributed into two seasons with positive trends: autumn (1.21 days decade^{-1}) and spring (0.49 days decade^{-1}). Significantly positive trends are also found for SE in summer (1.71 days decade^{-1}) and SCAN in autumn (1.44 days decade^{-1}). There are some negative trends, in particular for winter, but they are not significant for any region and season. Horton et al. (2014) reported a significant increase in air stagnation over some areas of the globe throughout the 21st century if greenhouse emissions remain unabated. One of the affected regions would be an area north of the Mediterranean covering most of SE and part of CEU, where we have also found upward trends. This suggests that an increase in stagnation may already have begun in some parts of Europe. According to that study, future increases in stagnation over the Mediterranean will result from more frequent dry days and stagnant 10 m wind occurrences, the first being associated with enhanced mid-tropospheric subsidence. We have also tried to assess the contribution of each individual ASI component to past annual trends by separately examining long-term changes in the occurrence of days when each individual component is below its stagnation threshold (Table 3). The contribution to the significant trends in CEU comes from the three ASI components, for which the occurrence of stagnant conditions has also experienced upward annual trends. For NEU there is only a significant rise in the occurrence of stagnant W_{10}. In the case of SE, the significant increase in the number of days with W_{500} below 13.0 m s^{-1} has led to an overall upward trend in stagnation, but this is partially counterbalanced by a substantial downward trend in DD. Similarly, the regions with weak trends (SCAN and SW) show changes of opposite signs in their individual components and such changes tend to cancel out. Summarizing, from the three ASI components, only the occurrence of W_{500} stagnant conditions has increased over most regions, and CEU and NEU are the only regions with upward trends in the three components. Nevertheless, the diverging results found for the different components and regions do not allow establishing clear conclusions on the drivers of long-term trends in stagnation over the whole area of study.

5 Synoptic patterns leading to stagnation

We have examined the synoptic patterns associated with stagnation in each cluster separately for summer and winter. Only summer and winter are analysed given that they are the seasons with the highest and lowest stagnation, as well as with the highest concentrations of O_3 and PM_{10} over most regions, respectively. Figure 5

displays the average Z500 anomalies for the five summers (left) and winters (right) with the largest number of stagnation days in each region. Likewise, SLP anomalies are shown in Fig. 6. There are at least five summers and winters when the number of stagnant days exceeds the seasonal mean plus one standard deviation for each region, which justifies the choice of the number of cases in each composite.

Different Z500 and SLP anomaly distributions can lead to above average stagnation, although we have identified two main patterns. Firstly, pattern H (high) is characterized by significantly positive anomalies in at least one of these fields over the region. This blocks the westerly flow, decreasing both near-surface and upper-air wind speed; concurrently, precipitation is also reduced within the region. Therefore, the three stagnation components more easily fulfil the air stagnation threshold condition when pattern H occurs. In Figures 5 and 6, this pattern can be identified in summer (left panels) for all regions with the exception of SW, and in winter for central and southern regions (CEU, SW and SE).

A second pattern denominated L (low) has been found for SCAN and NEU in winter. It consists of significantly negative anomalies of Z500 and SLP located south of the regions, together with significantly positive anomalies of Z500 over Greenland. This may displace the position of the Atlantic jet stream and consequently the storm tracks to the south, and, accordingly, yield an increase in stagnation over the north of the continent. We have checked that during the five winters with maximum stagnation over SCAN / NEU, the number of days with northern jet locations (53°-75° N) correspond to the 24^{th} / 30^{th} percentile of their winter climatology while the number of days with the jet in lower latitudes (15°-44° N) correspond to the 69^{th} / 71^{st} percentile, confirming our expectations.

We have not found any clear synoptic pattern associated with maximum stagnation over SW in summer. The Z500 anomaly maps for the five summers with most air stagnation in this region exhibit completely different patterns (i.e. anomalies are not spatially coincident, not shown), resulting in no clear pattern when the Z500 field is averaged for those summers.

6 Impact of air stagnation on air quality

We have assessed the impact of stagnation on air quality, focusing on winter PM_{10} and summer O_3. As the period with good data availability is different for both pollutants, we have evaluated PM_{10} from December 2002 to February 2011 and O_3 from 1998 to 2012. For the first exploratory analyses shown in Figure 7, the PM_{10} station data and the O_3 grid cells have been associated with the closest air stagnation grid cells at the nominal resolution of the reanalysis. The figure displays the difference between the seasonal concentrations of winter

PM_{10} (left) and summer O_3 (right) for days with and without stagnation. These anomalies are only shown when they are significant at the 95% confidence level (two-tailed t-test). As expected, there are widespread positive anomalies across the continent for both pollutants, although their magnitude varies depending on the region.

In the following, we will present some additional analyses to better understand the impact on the regions defined in Sect. 4 (Fig. 3). In these analyses, all grid cells within the region are considered for O_3 and only the background sites for PM_{10}, in order to avoid any potential biases in regions with a high proportion of traffic sites. It is known that the O_3 gridded dataset has some inhomogeneities around the Balkans before 2004 (Carro-Calvo et al., 2017); therefore, O_3 data within SE have only been considered since that year. The average anomalies (absolute values and percentages) of the pollutant concentrations on stagnant vs. non-stagnant days are summarized for each region in Table 4.

We first focus on the impact of air stagnation on winter PM_{10} (left panel of Fig. 7 and Table 4). The strongest effect is found for NEU and CEU. On average, PM_{10} concentrations are 16 μg m^{-3} higher on stagnant than on non-stagnant days in these clusters, which corresponds to more than half (58 and 56%) of the seasonal mean concentrations. The relative anomalies for the southern clusters (SW and SE) are above 30%, but these results should be treated with care due to the low number of sites. The impact over SCAN has not been considered due to the lack of PM_{10} data in this region. When averaged over all background sites in the five regions, the winter PM_{10} anomalies on stagnant days are above 15 μg m^{-3}, higher than those found by Garrido-Perez et al. (2017) over large areas of the continent under the influence of high-latitude blocks with centres located in the European sector (0˚-30˚ E).

Summer average O_3 anomalies (right panel of Fig. 7 and Table 4) are around 10 ppb (~20 μg m^{-3}) in CEU and above 5 ppb for three of the other four regions (NEU, SW and SE). These anomalies correspond to at least 13 % of the summer mean mixing ratios in each region (up to 23% in CEU). Such values are of the same order of magnitude as those reported by Ordóñez et al. (2017) for O_3 in different locations of Europe under the influence of high-latitude blocks and subtropical ridges. However, the ozone anomalies over SCAN on stagnant days are relatively small (5%) and lower than those found by that study under the influence of European blocks. The main reason for the relatively low anomalies of O_3 compared to those of PM_{10} during stagnant days most probably lies in the longer lifetime of the former, which implies a substantial contribution of transport processes and background concentrations to the atmospheric levels of this pollutant. It is also known that O_3 mixing ratios are enhanced over some regions of northern Europe following the advection of southern air masses (Carro-Calvo et al., 2017), which seems to be consistent with the moderate impact of stagnation found for SCAN and, to a

lesser extent, NEU, in comparison to CEU. In addition, a number of studies have attributed large-scale downward transport of ozone-rich air masses to elevated summer ozone in the lower troposphere over the Mediterranean (e.g. Velchev et al. 2011; Doche et al., 2014). This could be relevant for the SW and SE regions, but the air stagnation index does not implicitly include information on subsidence.

Taking these considerations into account, it is expected that the frequency distributions of both pollutants will also be affected by air stagnation. Figure 8 displays the probability density function (PDF) of daily PM_{10} (left) and O_3 (right) for the region most influenced by stagnation, i.e. CEU, considering all seasonal data (grey bars) as well as days with stagnation (red line). Both PDFs are displaced to the right on days with stagnation. There exists a reduction of the lower tails for both pollutants as well as an increase in the occurrence of daily PM_{10} concentrations above 30 μg m^{-3} and MDA8 O_3 mixing ratios above 45 ppb. This enlargement of the upper tails by air stagnation has clear implications for the number of exceedances of the 50 μg m^{-3} and 120 μg m^{-3} (~60 ppb) AQ limit values for these pollutants (indicated by vertical blue lines on both panels). Similar results, albeit with a more moderate impact, have been found for most of the other regions (see Supplementary Figures S2 and S3).

We have also examined the build-up of the pollutant concentrations during the most widespread stagnation events found in each region and season. To simplify the analyses, we have focused on the first five days of the ten episodes with the largest areal extent fulfilling stagnation conditions within each region and season (winter 2002-2011 and summer 1998-2012). We consider all background PM_{10} sites and O_3 grid cells within the region regardless of whether they are under stagnant conditions on those days. For illustration purposes, Figure 9 shows composites of the evolution of winter PM_{10} (top) and summer O_3 (bottom) during those episodes for CEU (left) and NEU (right). The first two boxes in each panel represent the distribution of the pollutant concentrations during the two days before the beginning of the episode (day0-2, day0-1) and the remaining boxes correspond to the first five days of the event (day0, day0+1, day0+2, day0+3, day0+4). As the extension of the stagnant area increases day after day for some of the ten episodes considered and decreases for others, this may result in large spread in the data and even decreases in the median concentrations during the life cycles of these episodes.

The PM_{10} build-up during the winter episodes (Figure 9, top) is particularly pronounced for NEU, even though only slightly above 20% of the region is under stagnant conditions during those events, compared to above 35% for CEU. The median of the PM_{10} concentrations increases by nearly 20 μg m^{-3} from day0-2 to day0+3 in CEU, while there is a stronger build-up of ~20 μg m^{-3} during the first three days (day0 to day0+2) in NEU. Nevertheless,

476 the upper quartiles (top of the boxes) considerably exceed 50 μg m^{-3} during the five days of the episodes in
477 CEU, indicating that at least 25% of the background sites in the region breach the air quality target for this
478 pollutant. This also occurs in NEU, but only from the third day of the episodes (day0+2 to day0+4). In the case
479 of summer O_3 (Figure 9, bottom), the percentage of the region under stagnant conditions during the selected
480 events is above 40 % in CEU and 30 % in NEU. There is a strong increase (> 15 ppb) in the median O_3
481 concentrations over CEU from day0-1 to day0+4 and the upper quartiles, i.e. 25% of the sites, exceed the 60
482 ppb threshold from day0+2 to day0+4. The build-up of O_3 over NEU is not as strong, with a steady increase in
483 the median concentrations of ~6 ppb only from day0-1 to day0+1. In both cases there is also a remarkable rise
484 in the low percentiles (lower whiskers) throughout the episodes, indicating a widespread impact of air stagnation
485 on the sites with the lowest O_3 concentrations within these two regions. Overall, similar life cycles, although with
486 a more moderate impact, have been found for PM_{10} and O_3 during stagnation episodes in the other regions
487 (Supplementary Figures S4 and S5). Consequently, persistent air stagnation conditions facilitate the build-up of
488 both pollutants in the area of study.
489 Finally, we have investigated whether the frequency of occurrence of air stagnation can determine the
490 interannual variability of summer O_3 extremes (defined as the 95th percentiles of the seasonal concentrations),
491 in a similar way as done by Schnell and Prather (2017) for eastern US. The analysis has been conducted only
492 for the regions with good spatiotemporal coverage of O_3 (i.e. all regions except for SE). We have not considered
493 PM_{10} due to the relatively short time series (only 9 winters) available for this pollutant. The time series have
494 been detrended by subtracting the year-to-year change expected from a linear trend (using ordinary least
495 squares regression). The coefficients of correlation are 0.54 for SCAN, 0.72 for NEU, 0.81 for CEU and 0.58 for
496 SW. Overall, the link between the interannual variability of air stagnation and O_3 extremes in Europe is similar
497 to that reported by Schnell and Prather (2017) for a larger region in the US during the extended summer season,
498 with R values of 0.79. This is particularly the case for O_3 in CEU and NEU. The corresponding time series are
499 shown in Figure 10. It is worthwhile to mention the high percentage of stagnation days in the summers with the
500 highest ozone levels: summer 2003 for CEU and summer 2006 in NEU. These two summers were indeed
501 periods of exceptionally hot weather and extreme air pollution over different parts of Europe, as reported by
502 other studies (e.g. Schnell et al., 2014; Carro-Calvo et al., 2017, and references therein). Therefore, our results
503 demonstrate that a simple linear model on the frequency of stagnant days can explain a considerable fraction
504 of the interannual variability of summer ozone extremes, and suggest that air stagnation may also be a good
505 indicator of some meteorological extremes such as heatwaves. This is in line with previous studies that have

highlighted the joint association of high ozone and temperature with stagnation. While it has been consistently observed that summer ozone correlates with temperature, this is not only driven by the impact of temperature on photochemical ozone production (e.g. through the thermal decomposition of the reservoir species peroxyacetyl nitrate and the increase in emissions of biogenic isoprene at high temperatures), as it also reflects the association of high temperatures with air mass origin and regional stagnation (Jacob et al., 1993; Jacob and Winner, 2009, and references therein).

7 Summary and conclusions

Previous studies have either used reanalysis (e.g. Wang and Angell, 1999), climate models (Horton et al., 2012, 2014) or observations (e.g. Huang et al., 2017) to quantify air stagnation. We have provided a comprehensive characterization of air stagnation over Europe for the 1979–2016 period by using a simplified air stagnation index (ASI) which tags stagnant conditions as those when daily accumulated precipitation and near-surface and upper wind speed are simultaneously below predefined thresholds (Horton et al., 2012). To the author's knowledge, this study presents the first comparison of stagnation as derived both from observations and reanalysis. For that purpose, we have used daily 10 m and upper wind speeds as well as precipitation data from the ISD, IGRA and E-OBS observational datasets, respectively, together with ERA-Interim reanalysis data. Our findings indicate a reasonably good agreement between reanalysis and observations in the representation of the frequency and variability of stagnation days and events at the regional scale. Overall, both the occurrence of dry days and stagnant upper air wind speed are consistent between reanalysis and observations, while the 10 m wind speed is responsible for the main differences due to its dependence on local factors, including the orography and surface roughness, as well as the insufficient horizontal resolution and imperfect parameterizations of the reanalysis.

There is considerable spatial heterogeneity across Europe, with more stagnation in the south than in the north. Thus, we have regionalized the Euro-Mediterranean region through the application of the k-means clustering technique to the monthly frequency of stagnant days considering all reanalysis grid cells. This has allowed us to distinguish five regions with different behaviour: Scandinavia (SCAN), Northern Europe (NEU), Central Europe (CEU), South West (SW) and South East (SE). The temporal variability, the associated large scale circulation patterns and the impact on the atmospheric concentrations of two pollutants (PM_{10} and O_3) have then been studied separately for each region. Table 5 summarizes this information for winter and summer.

The regions located at higher latitudes, SCAN and NEU, present the lowest stagnation frequency. Ample precipitation and high 10 m winds are respectively the limiting factors to the occurrence of stagnation in these regions. The role of 10 m winds is particularly relevant in the case of NEU as it includes the regions around the North and Baltic Seas, where near-surface westerlies prevail. Both regions share some common features such as small amplitude of the seasonal cycle and low interannual variability. The synoptic patterns that maximize stagnation are also common to both regions. In summer, they are characterized by positive anomalies of Z500 over the region (labelled as pattern H). Unlike other regions, the winter synoptic patterns ruling stagnation display positive anomalies over Greenland and a southward displacement of the jet (pattern L). Air stagnation is associated with strong positive anomalies of winter PM_{10} in NEU and moderate summer O_3 anomalies in both regions, standing out as a relatively good indicator for interannual variability of extreme ozone events, with correlations of 0.54 and 0.72 for SCAN and NEU, respectively.

The highest frequency of stagnation occurs over the Mediterranean area, where the seasonal cycle is characterized by a maximum in summer and high interannual variability. This area is comprised of two distinct regions (SW and SE), for which the major limiting factor to the occurrence of stagnant conditions is upper wind speed. This component also drives part of the interannual variability of stagnation in both regions, in particular over SW. Despite these similarities, the frequency of dry days is lower in SE and therefore considerably contributes to the interannual variability of stagnation in this region. On seasonal scales, maximum stagnation in these regions is often associated with pattern H, although no clear synoptic pattern has been found for SW in summer. The impact on AQ is noteworthy but somewhat weaker than in other European regions. Nevertheless, some caution is required due to the limited number of sites for both regions.

Finally, CEU is the region that covers most of continental Europe and presents moderate stagnation. The interannual variability is relatively small, as does the seasonal cycle, with a slight rise in autumn. CEU is a transition region between the south and the north. As such, different components (namely, upper air winds and dry days) dominate the interannual variability of stagnation. This is also the region with the largest annual trends (+2.38 days $decade^{-1}$) and similar upward values are separately found for the three ASI components. CEU also stands out as the region where stagnation has the largest impact on AQ, with relative anomalies above 20% for summer O_3 and 50% for winter PM_{10}. Furthermore, exceedances of AQ targets for these two pollutants are more likely to occur on stagnant days. In particular, the stronger impact on the first pollutant in CEU compared to the remaining clusters might be related to the fact that other factors are known to contribute to elevated summer ozone in those regions, namely southerly advection in northern Europe (Carro-Calvo et al., 2017) and

large scale subsidence in the proximity of the Mediterranean (e.g. Velchev et al. 2011; Doche et al., 2014; Zanis et al., 2014). A better understanding of these dynamical processes would be useful to develop more sophisticated meteorological indices for those regions. In spite of that, our analyses have proved that persistent, widespread stagnation events favour the build-up of both O_3 and PM_{10} over most of the continent.

In short, our results demonstrate the usefulness of a simple ASI to characterize the spatiotemporal variability of air stagnation and represent the conditions favourable for the accumulation of PM and O_3 over the Euro-Mediterranean area. We have been able to identify regions where stagnation behaves differently and consequently so do features such as the temporal variability, the associated large-scale circulation patterns and the impact on AQ. These findings confirm that air stagnation triggers elevated concentrations of air pollutants over most regions of Europe, including the occurrence of AQ episodes. The results reported herein will hopefully motivate observational and regional modelling studies aimed to better understand the dynamics of air stagnation and its role in AQ episodes.

Acknowledgements

This study was carried out under the aegis of a predoctoral research grant awarded by the Spanish Ministerio de Educación, Cultura y Deporte (FPU16/01972) and the support of the Ramón y Cajal Programme of the Spanish Ministerio de Economía y Competitividad [grant number RYC-2014-15036]. The work is also supported by the Spanish Ministry of Economy, Industry and Competitiveness trough project CGL2017-83198-R, "Variabilidad Climática y mecanismos dinámicos de los episodios de estancamiento atmosférico en la región euro-mediterránea". We thank J. L. Schnell, the European Monitoring and Evaluation Programme (EMEP) and the European Environment Agency (EEA) for providing the air quality data sets used in this study. We acknowledge the E-OBS dataset from the EU-FP6 project ENSEMBLES (http://ensembles-eu.metoffice.com, last access: March 2018) and the data providers in the ECA&D project (http://www.ecad.eu, last access: March 2018). ERA-Interim data provided courtesy ECMWF. NCEP/NCAR reanalysis data are provided by the NOAA/OAR/ESRL PSD, Boulder, Colorado, USA, from their web site at http://www.esrl.noaa.gov/psd/. The authors also acknowledge NCDC for providing IGRA radiosonde and ISD near-surface wind data.

589 **References**

590 Aurenhammer, F.: Voronoi Diagrams - a Survey of a Fundamental Geometric Data Structure. ACM Comput.
591 Surv. 23(1), 345–405, doi:10.1145/116873.116880, 1991.
592 Bador, M., Naveau, P., Gilleland, E., Castellà, M. and Arivelo, T.: Spatial clustering of summer temperature
593 maxima from the CNRM-CM5 climate model ensembles & E-OBS over Europe. Weather Clim. Extrem., 9, 17-
594 24, doi:10.1016/j.wace.2015.05.003, 2015.
595 Brown, B. G., E. Gilleland and E. E. Ebert: Forecasts of spatial fields, in Forecast Verification A Practitioner's
596 Guide in Atmospheric Science, Second Edition, I. T. Jolliffe and D. B. Stephenson Eds., John Wiley & Sons
597 Ltd., ISBN: 978-0-470-66071-3, 2012.
598 Brunner, D., Jorba, O., Savage, N., Eder, B., Makar, P., Giordano, L., Badia, A., Balzarini, A., Baro, R., Bianconi,
599 R., Chemel, C., Forkel, R., Jimenez-Guerrero, P., Hirtl, M., Hodzic, A., Honzak, L., Im, U., Knote, C., Kuenen,
600 J. J. P., Makar, P. A., MandersGroot, A., Neal, L., Perez, J. L., Pirovano, G., San Jose, R., Savage, N., Schroder,
601 W., Sokhi, R. S., Syrakov, D., Torian, A., Werhahn, K., Wolke, R., van Meijgaard, E., Yahya, K., Zabkar, R.,
602 Zhang, Y., Zhang, J., Hogrefe, C., and Galmarini, S.: Comparative analysis of meteorological performance of
603 coupled chemistry-meteorology models in the context of AQMEII phase 2, Atmos. Environ., 115, 470–498,
604 doi:10.1016/j.atmosenv.2014.12.032, 2015.
605 Cai, W., K. Li, H. Liao, H. Wang and L. Wu: Weather conditions conducive to Beijing severe haze more frequent
606 under climate change, Nat. Clim. Change, 7(4), 257-262, doi:10.1038/NCLIMATE3249, 2017.
607 Carro-Calvo, L., Ordóñez, C., García-Herrera, R. and Schnell, J. L.: Spatial clustering and meteorological drivers
608 of summer ozone in Europe, Atmos. Environ., 167, 496–510, doi:10.1016/j.atmosenv.2017.08.050, 2017.
609 Carvalho, M.J., Melo-Gonçalves, P., Teixeira, J.C. and Rocha, A.: Regionalization of Europe based on a K-
610 Means Cluster Analysis of the climate change of temperatures and precipitation. Phys. Chem. Earth, 94, 22-28.
611 http://dx.doi.org/10.1016/j.pce.2016.05.001, 2016.
612 Caserini, S., Giani, P., Cacciamani, C., Ozgen, S. and Lonati, G.: Influence of climate change on the frequency
613 of daytime temperature inversions and stagnation events in the Po Valley: historical trend and future
614 projections. Atmos. Res., 184, 15-23, doi:10.1016/j.atmosres.2016.09.018, 2017.
615 Dawson, J. P., Bloomer, B. J., Winner, D. A. and Weaver, C. P.: Understanding the meteorological drivers of
616 U.S. particulate matter concentrations in a changing climate, Bull. Am. Meteorol. Soc., 95(4), 521–532,
617 doi:10.1175/BAMS-D-12-00181.1, 2014.

618 Dee, D. P., Uppala, S. M., Simmons, A. J., Berrisford, P., Poli, P., Kobayashi, S., Andrae, U., Balmaseda, M.
619 A., Balsamo, G., Bauer, P., Bechtold, P., Beljaars, A. C. M., van de Berg, L., Bidlot, J., Bormann, N., Delsol, C.,
620 Dragani, R., Fuentes, M., Geer, A. J., Haimberger, L., Healy, S. B., Hersbach, H., Hólm, E. V., Isaksen, L.,
621 Kållberg, P., Köhler, M., Matricardi, M., Mcnally, A. P., Monge-Sanz, B. M., Morcrette, J. J., Park, B. K., Peubey,
622 C., de Rosnay, P., Tavolato, C., Thépaut, J. N. and Vitart, F.: The ERA-Interim reanalysis: Configuration and
623 performance of the data assimilation system, Q. J. Roy. Meteorol. Soc., 137(656), 553–597, doi:10.1002/qj.828,
624 2011.
625 Doche, C., Dufour, G., Foret, G., Eremenko, M., Cuesta, J., Beek- mann, M. and Kalabokas, P.: Summertime
626 tropospheric-ozone variability over the Mediterranean basin observed with IASI, Atmos. Chem. Phys., 14,
627 10589–10600, doi:10.5194/acp-14- 10589-2014, 2014.
628 Durre, I., Vose, R. S. and Wuertz, D. B.: Overview of the Integrated Global Radiosonde Archive, J. Clim., 19,
629 53-68, doi:10.1175/JCLI3594.1, 2006.
630 Garrido-Perez, J. M., Ordóñez, C. and García-Herrera, R.: Strong signatures of high-latitude blocks and
631 subtropical ridges in winter PM10 over Europe, Atmos. Environ., 167, 49–60,
632 doi:10.1016/j.atmosenv.2017.08.004, 2017.
633 Gatey, D., Isyumov, N., Case, P., Ho, T. E. and Miller, C.: Design wind climates for very tall structures, in:
634 Proceedings of the 13th International Conference on Wind Engineering, Amsterdam, The Netherlands, 10-15
635 June 2011, 2011.
636 Haylock, M., Hofstra, N., Klein Tank, A., Klok, E., Jones, P. and New, M.: A European daily high-resolution
637 gridded dataset of surface temperature and precipitation for 1950-2006, J. Geophys. Res., 113 (D20),
638 doi:10.1029/2008JD010201, 2008.
639 Horton, D. E., Harshvardhan and Diffenbaugh, N. S.: Response of air stagnation frequency to anthropogenically
640 enhanced radiative forcing, Environ. Res. Lett., 7(4), 044034, doi:10.1088/1748-9326/7/4/044034, 2012.
641 Horton, D. E., Skinner, C. B., Singh, D. and Diffenbaugh, N. S.: Occurrence and persistence of future
642 atmospheric stagnation events, Nat. Clim. Chang., 4(8), 698–703, doi:10.1038/nclimate2272, 2014.
643 Huang, Q., Cai, X., Song, Y. and Zhu, T.: Air stagnation in China (1985 – 2014): climatological mean features
644 and trends, Atmos. Chem. Phys., 17, 7793–7805, doi:10.5194/acp-17-7793-2017, 2017.
645 Huang, Q., Cai, X., Wang, J., Song, Y. and Zhu, T.: Climatological study of the Boundary-layer air Stagnation
646 Index for China and its relationship with air pollution, Atmos. Chem. Phys., 18, 7573-7593, doi:10.5194/acp-18-
647 7573-2018, 2018.

Jacob, D. J., Logan, J. A., Gardner, G. M., Yevich, R. M., Spivakovsky, C. M., Wofsy, S. C., Sillman, S., Prather, M. J.: Factors regulating ozone over the United States and its export to the global atmosphere, J. Geophys. Res. 98, 14817–14826, 1993.

Jacob, D. J. and Winner, D. A.: Effect of climate change on air quality, Atmos. Environ., 43, 51-63, doi: 10.1016/j.atmosenv.2008.09.051, 2009.

Kalnay, E., Kanamitsu, M., Kistler, R., Collins, W., Deaven, D., Gandin, L., Iredell, M., Saha, S., White, G., Woollen, J., Zhu, Y., Chelliah, M., Ebisuzaki, W., Higgins, W., Janowiak, J., Mo, K. C., Ropelewski, C., Wang, J., Leetmaa, A., Reynolds, R., Jenne, R., and Joseph, D.: The NMC/NCAR 40-Year Reanalysis Project, B. Am. Meteorol. Soc., 77, 437–471, 1996.

Koelemeijer, R. B. A., Homan, C. D. and Matthijsen, J.: Comparison of spatial and temporal variations of aerosol optical thickness and particulate matter over Europe. Atmos. Env., 40(27), 5304-5315, doi:10.1016/j.atmosenv.2006.04.044, 2006.

Korshover, J. and Angell, J.: A review of air-stagnation cases in the eastern United States during 1981-Annual Summary, Mon. Weather Rev., 110, 1515–1519, doi:10.1175/1520-0493(1982)110<1515:AROASC>2.0.CO;2, 1982.

Laurila, T.: Observational study of transport and photochemical formation of ozone over northern Europe, J. Geophys. Res., 104, 26235–26243, doi:10.1029/1999JD900772, 1999.

Leibensperger, E. M., Mickley, L. J. and Jacob, D. J.: Sensitivity of US air quality to mid-latitude cyclone frequency and implications of 1980–2006 climate change, Atmos. Chem. Phys., 8(23), 7075–7086, doi:10.5194/acp-8-7075-2008, 2008.

Lyapina, O., Schultz, M. G., and Hense, A.: Cluster analysis of European surface ozone observations for evaluation of MACC reanalysis data, Atmos. Chem. Phys., 16, 6863-6881, doi:10.5194/acp-16-6863-2016, 2016.

Nygard, T., Valkonen, T. and Vihma, T.: Characteristics of Arctic low-tropospheric humidity inversions based on radio soundings, Atmos. Chem. Phys., 14(4), 1959-1971, doi:10.5194/acp-14-1959-2014, 2014.

Ordóñez, C., Barriopedro, D., García-Herrera, R., Sousa, P. M. and Schnell, J. L.: Regional responses of surface ozone in Europe to the location of high-latitude blocks and subtropical ridges, Atmos. Chem. Phys., 17(4), 3111–3131, doi:10.5194/acp-17-3111-2017, 2017.

Otero, N., Sillmann, J., Schnell, J. L., Rust, H. W. and Butler, T.: Environmental Research Letters Synoptic and meteorological drivers of extreme ozone concentrations over Europe Synoptic and meteorological drivers of extreme ozone concentrations over Europe, Environ. Res. Lett, 11, doi:10.1088/1748-9326/11/2/024005, 2016.

Schnell, J. L. and Prather, M. J.: Co-occurrence of extremes in surface ozone, particulate matter, and temperature over eastern North America, Proc. Natl. Acad. Sci., 114(11), 2854–2859, doi:10.1073/pnas.1614453114, 2017.

Schnell, J. L., Holmes, C. D., Jangam, A. and Prather, M. J.: Skill in forecasting extreme ozone pollution episodes with a global atmospheric chemistry model, Atmos. Chem. Phys., 14(15), 7721–7739, doi:10.5194/acp-14-7721-2014, 2014.

Schnell, J. L., Prather, M. J., Josse, B., Naik, V., Horowitz, L. W., Cameron-Smith, P., Bergmann, D., Zeng, G., Plummer, D. A., Sudo, K., Nagashima, T., Shindell, D. T., Faluvegi, G. and Strode, S. A.: Use of North American and European air quality networks to evaluate global chemistry-climate modeling of surface ozone, Atmos. Chem. Phys., 15(18), 10581–10596, doi:10.5194/acp-15-10581-2015, 2015.

Smith, A., Lott, N. and Vose, R.: The integrated surface database: Recent developments and partnerships, Bull. Am. Meteorol. Soc., 92(6), 704–708, doi:10.1175/2011BAMS3015.1, 2011.

Sun, W., Hess, P. and Liu, C.: The impact of meteorological persistence on the distribution and extremes of ozone, Geophys. Res. Lett., 44(3), 1545–1553, doi:10.1002/2016GL071731, 2017.

Tai, A. P. K., Mickley, L. J. and Jacob, D. J.: Correlations between fine particulate matter (PM2.5) and meteorological variables in the United States: Implications for the sensitivity of $PM_{2.5}$ to climate change, Atmos. Environ., 44(32), 3976–3984, doi:10.1016/j.atmosenv.2010.06.060, 2010.

Torrence, C. and Compo, G. P.: A practical guide to wavelet analysis. Bull. Am. Meteorol. Soc., 79(1), 61-78, doi:10.1175/1520-0477(1998)079<0061:APGTWA>2.0.CO;2, 1998.

Tørseth, K., Aas, W., Breivik, K., Fjeraa, A. M., Fiebig, M., Hjellbrekke, A. G., Lund Myhre, C., Solberg, S. and Yttri, K. E.: Introduction to the European Monitoring and Evaluation Programme (EMEP) and observed atmospheric composition change during 1972-2009, Atmos. Chem. Phys., 12(12), 5447–5481, doi:10.5194/acp-12-5447-2012, 2012.

Vautard, R., Cattiaux, J., Yiou, P., Thépaut, J. N. and Ciais, P.: Northern Hemisphere atmospheric stilling partly attributed to an increase in surface roughness, Nat. Geosci., 3(11), 756–761, doi:10.1038/ngeo979, 2010.

Velchev, K., Cavalli, F., Hjorth, J., Marmer, E., Vignati, E., Dentener, F., and Raes, F.: Ozone over the Western Mediterranean Sea – results from two years of shipborne measurements, Atmos. Chem. Phys., 11, 675-688, doi:10.5194/acp-11-675-2011, 2011.

Wang, J. X. L. and Angell, J. K.: Air Stagnation Climatology for the United States (1948-1998), NOAA/Air Resources Laboratory ATLAS, 1, 1999.

Wang, X., Wang, K. and Su, L.: Contribution of Atmospheric Diffusion Conditions to the Recent Improvement in Air Quality in China, Sci. Rep., 6, 1–11, doi:10.1038/srep36404, 2016.

Wang, X., Dickinson, R. E., Su, L., Zhou, C., Wang, K., Wang, X., Dickinson, R. E., Su, L., Zhou, C. and Wang, K.: PM2.5 Pollution in China and How It Has Been Exacerbated by Terrain and Meteorological Conditions, Bull. Am. Meteorol. Soc., BAMS-D-16-0301.1, doi:10.1175/BAMS-D-16-0301.1, 2017.

Woollings, T., Hannachi, A. and Hoskins, B.: Variability of the North Atlantic eddy-driven jet stream, Q. J. Royal Meteorol. Soc., 136(649), 856-868, doi:10.1002/qj.625, 2010.

Xu, L., Yu, J.-Y., Schnell, J. L. and Prather, M. J.: The seasonality and geographic dependence of ENSO impacts on U.S. surface ozone variability, Geophys. Res. Lett., 44, 3420–3428, doi:10.1002/2017GL073044, 2017.

Zanis, P., Hadjinicolaou, P., Pozzer, A., Tyrlis, E., Dafka, S., Mi- halopoulos, N. and Lelieveld, J.: Summertime free-tropospheric ozone pool over the eastern Mediterranean/Middle East, Atmos. Chem. Phys., 14, 115–132, doi:10.5194/acp-14-115-2014, 2014.

Zou, Y., Wang, Y., Zhang Y. and Koo, J-H.: Arctic sea ice, Eurasia snow, and extreme winter haze in China, Sci. Adv., 3(3), e1602751, doi:10.1126/sciadv.1602751, 2017.

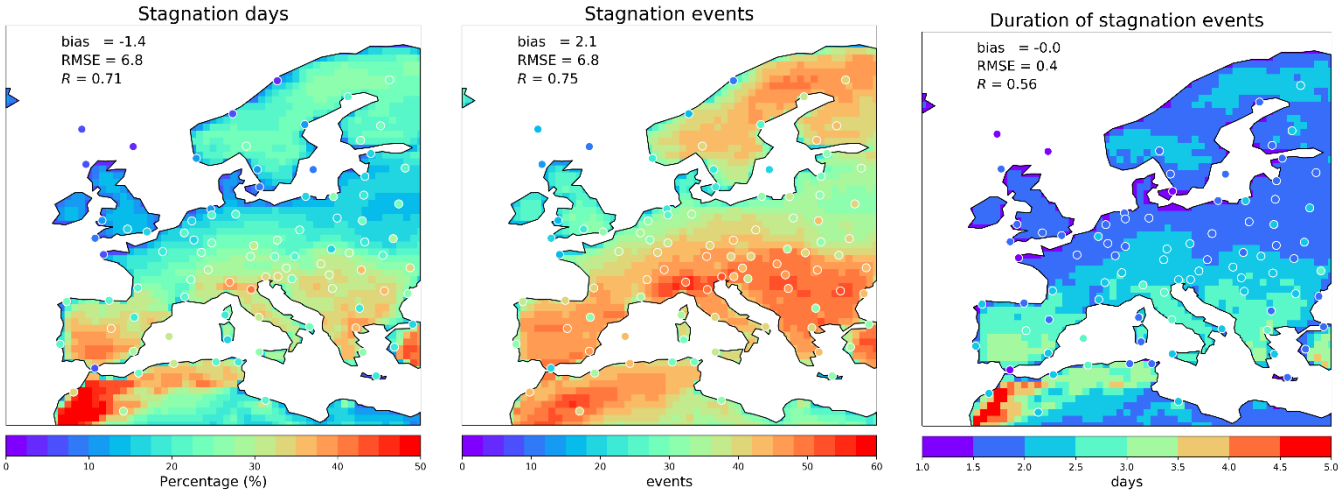

724

725 **Figure 1: Percentage of stagnation days (%, left) and average number of stagnation events per year (middle), and**
726 **mean event duration (number of days, right) during the period 1979-2016. Shaded colours represent reanalysis data**
727 **and coloured circles observations. Mean bias (MB), root mean square error (RMSE) and Pearson correlation**
728 **coefficient (R) are obtained from the two samples considering only the grid cells of the reanalysis which are closest**
729 **to the observational sites.**

730

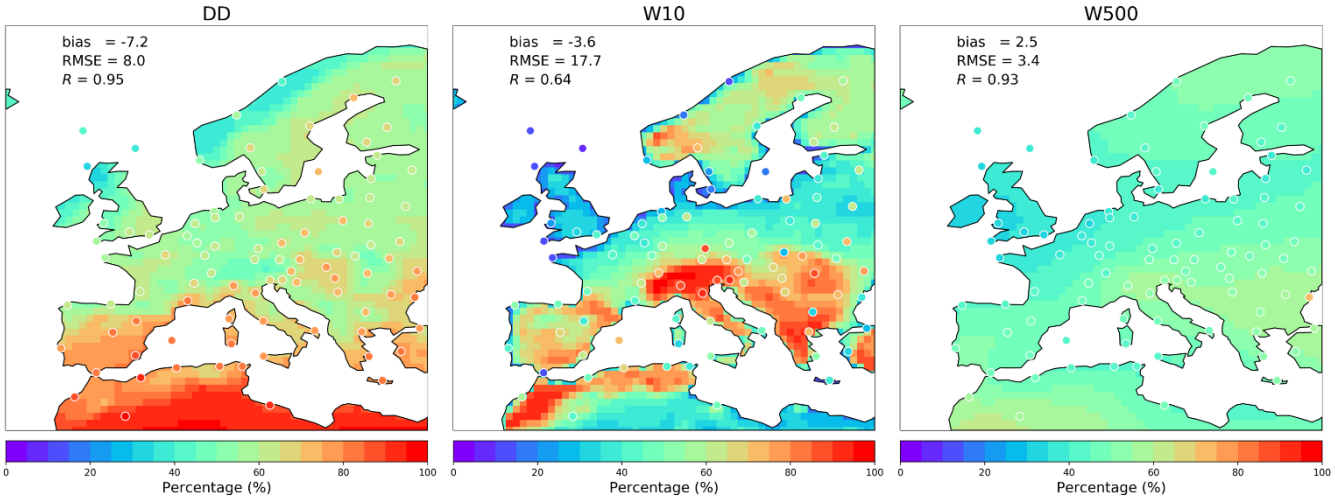

731

732 **Figure 2: Annual percentage of days that fulfil the stagnation condition for precipitation (left), 10 m wind speed**
733 **(middle) and upper-air wind speed (right) during the period 1979-2016. Shaded colours represent reanalysis and**
734 **coloured circles observations. Mean bias (%), root mean square error (RMSE, %) and correlation coefficient (R) are**
735 **obtained from the two samples considering only the grid cells of the reanalysis which are closest to the**
736 **observations.**

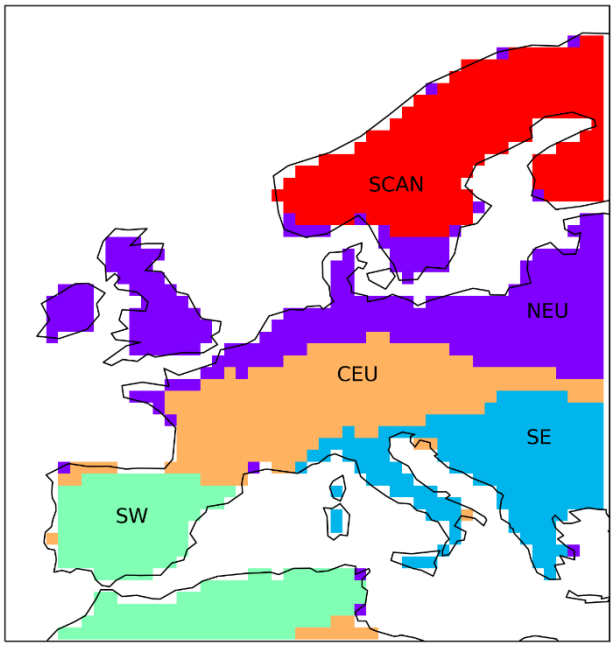

Figure 3: Regionalization of the monthly frequency of air stagnation during 1979-2016, as derived from the ERA-Interim reanalysis. Coloured shading identifies the clustered regions, which broadly correspond to Scandinavia (SCAN), Northern Europe (NEU), Central Europe (CEU), South West (SW) and South East (SE).

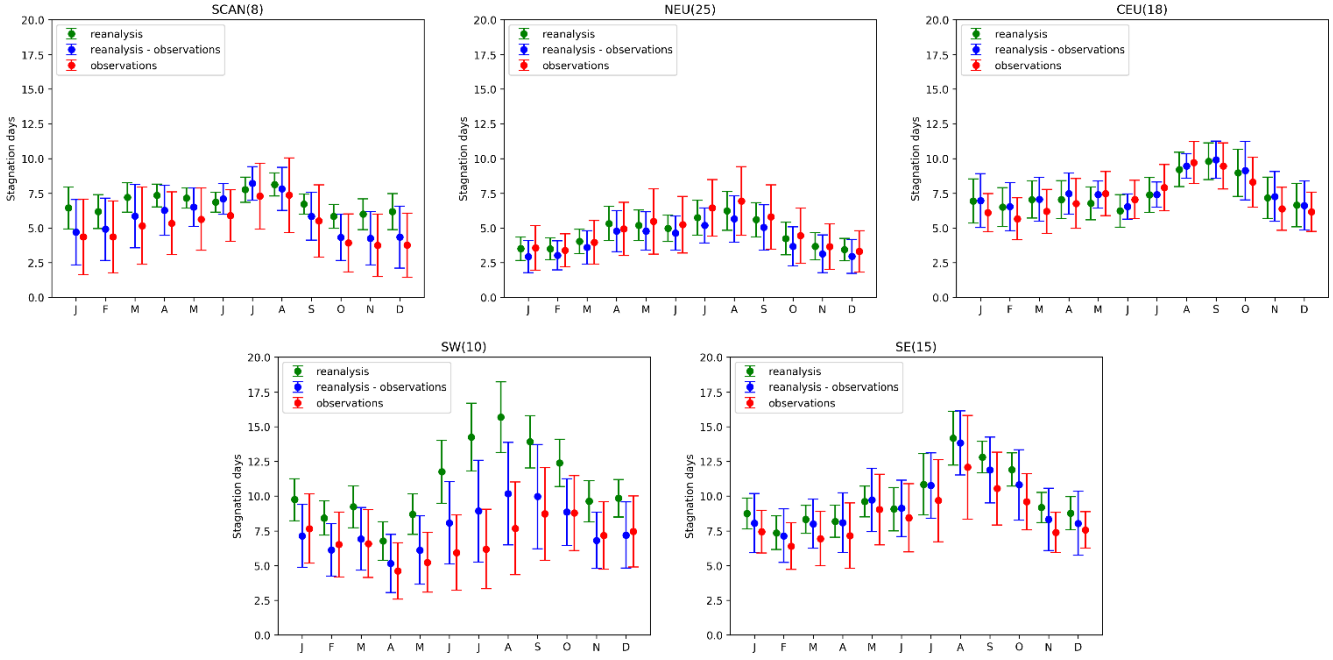

Figure 4: Seasonal cycles of the monthly frequency of stagnation days for each of the clusters shown in Figure 3. They are calculated from observations (red), reanalysis considering the closest grid cells to observations (blue) and all the grid cells (green) for a given region. The filled circles represent the mean values and the error bars extend from the mean to show the range of the data $\pm$ one standard deviation (SD). Each SD has been calculated for the 38 monthly values of each location during the period of analysis (1979-2016). The numbers in brackets represent the number of stations considered in each cluster.

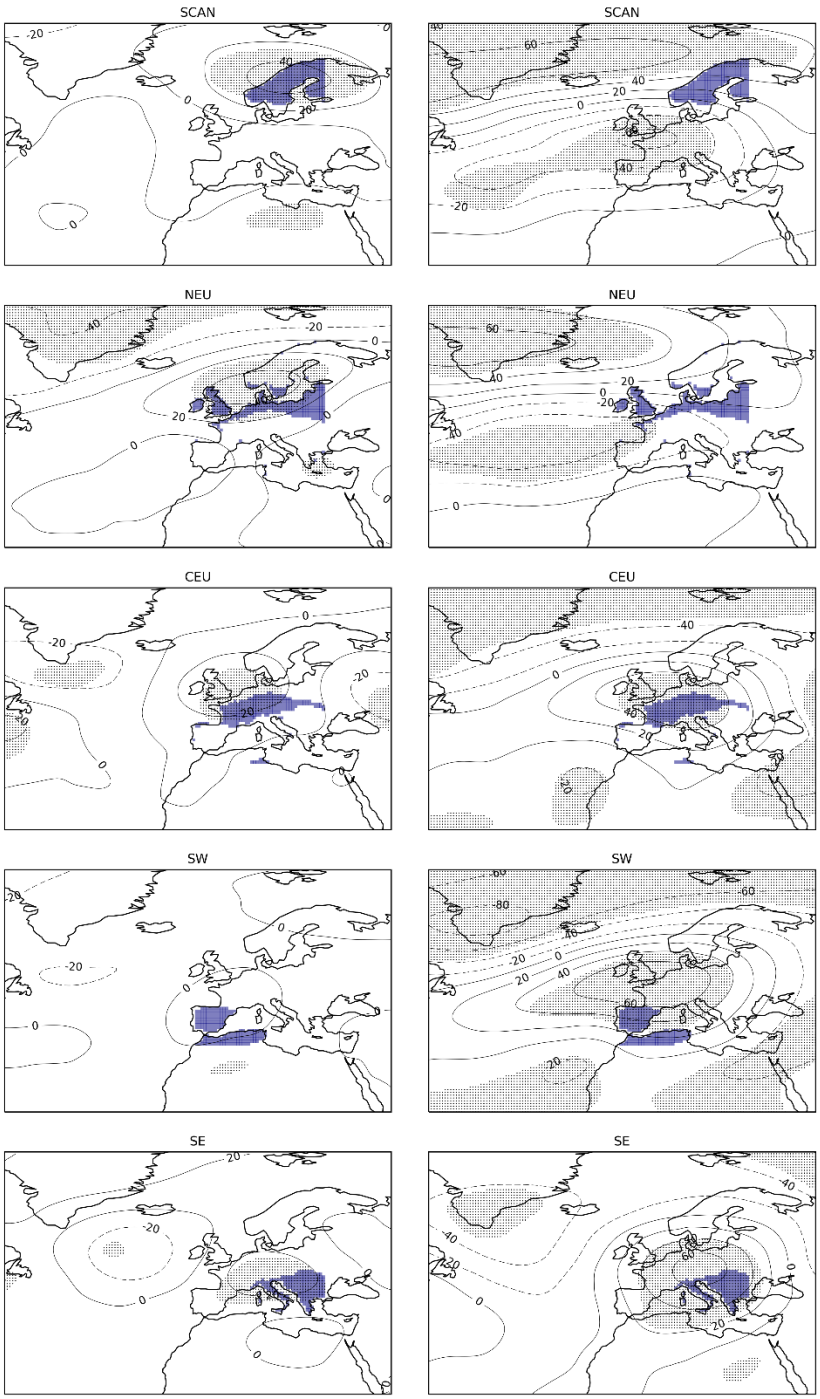

Figure 5: Composite anomalies of 500 hPa geopotential height (m; lines) for the 5 summers (left) and winters (right) with the largest number of stagnation days in each region. The regions, from top to bottom, are SCAN, NEU, CEU, SW and SE. Blue shading depicts the location of the region and stippling the areas where anomalies are significant at the 95% confidence level. Anomalies have been calculated with respect to the seasonal climatology during the 1979–2016 period.

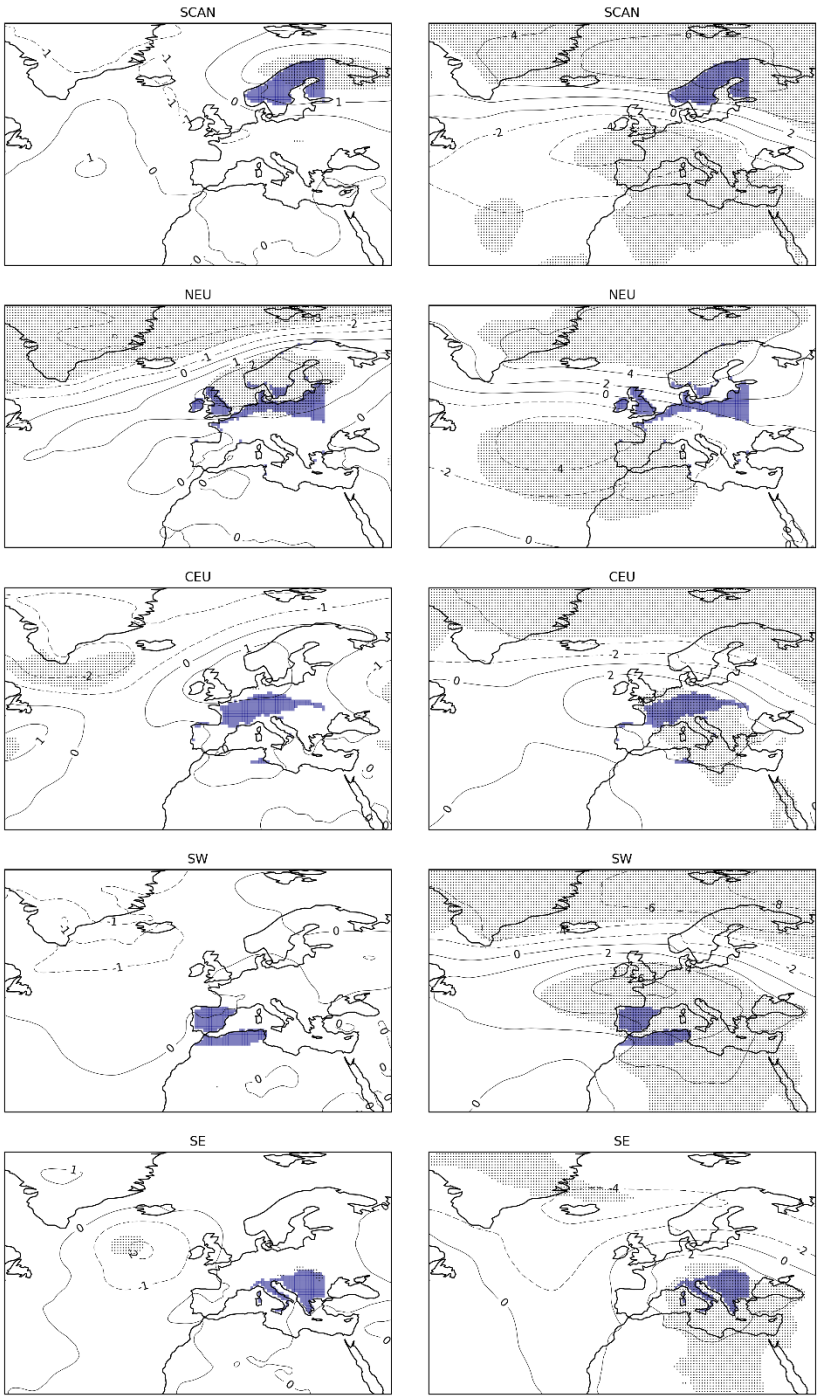

Figure 6: As Figure 5 but for SLP, represented by line contours at 1 hPa intervals in summer and 2 hPa in winter.

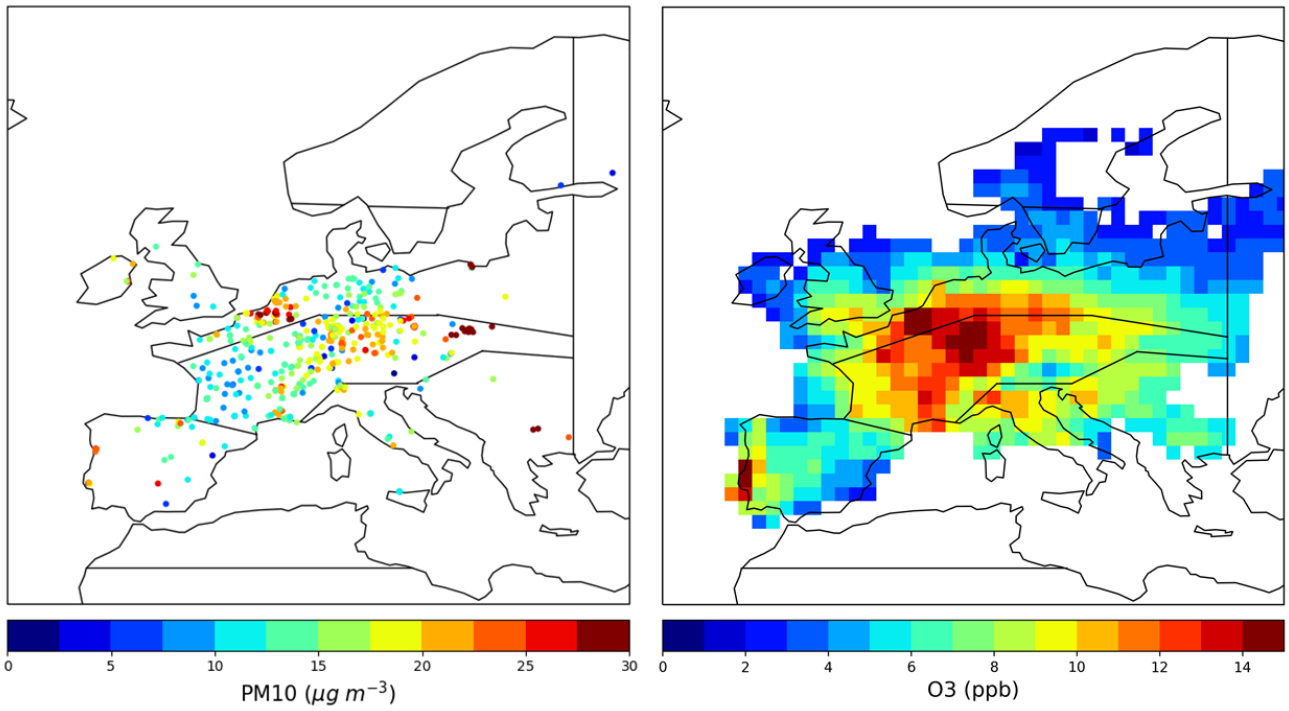

Figure 7: Composites of winter PM_{10} (µg m^{-3}, left) and summer O_3 (ppb, right) concentration anomalies on days with stagnation, with respect to the days without stagnation during the same season. PM_{10} data have been evaluated for Dec 2002 – Feb 2011 and O_3 for 1998-2012. Anomalies are only shown when they are statistically significant at the 95% confidence level (determined through a two-tailed t-test). The boundaries on the maps roughly correspond to those of the five clusters: SCAN, NEU, CEU, SW and SE.

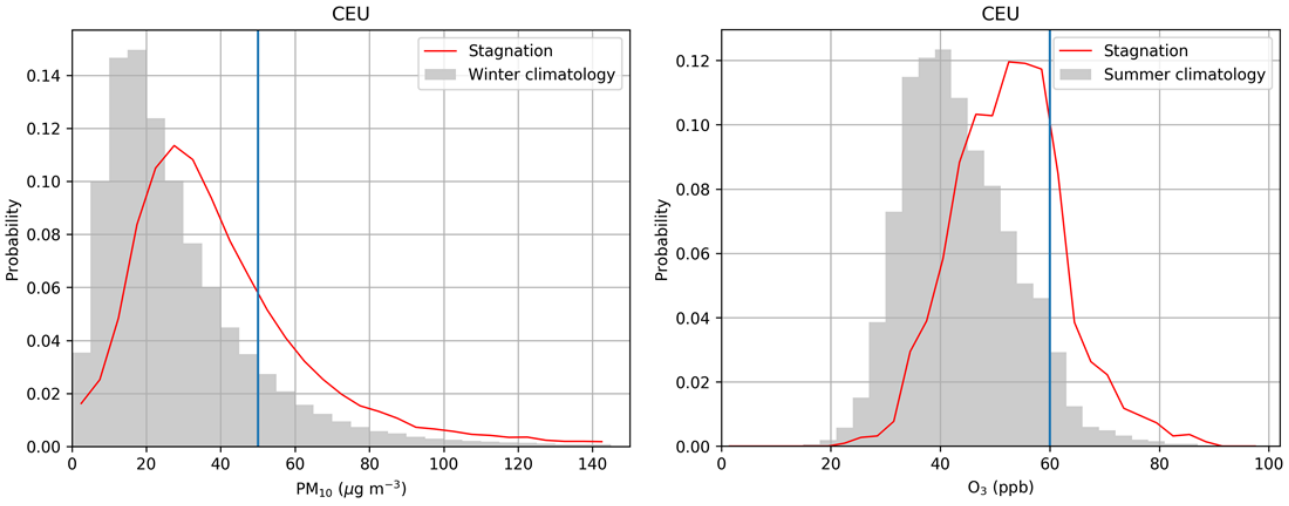

Figure 8: Probability density functions (PDFs) of daily winter background PM_{10} concentrations (µg m^{-3}, left) and summer MDA8 ozone mixing ratios (ppb, right) for CEU. Grey bars correspond to the histogram considering all seasonal data. Red lines represent the distribution considering only days with stagnation. These PDFs are significantly different at the 95% confidence level for both pollutants (determined through a two-sample

Kolmogorov-Smirnov test). Each bin covers a range of 5 µg m^{-3} for PM_{10} and 3 ppb for O_3. The vertical lines at 50 µg m^{-3} and 60 ppb represent the air quality targets for PM_{10} averaged over 24 h and for MDA8 O_3, respectively.

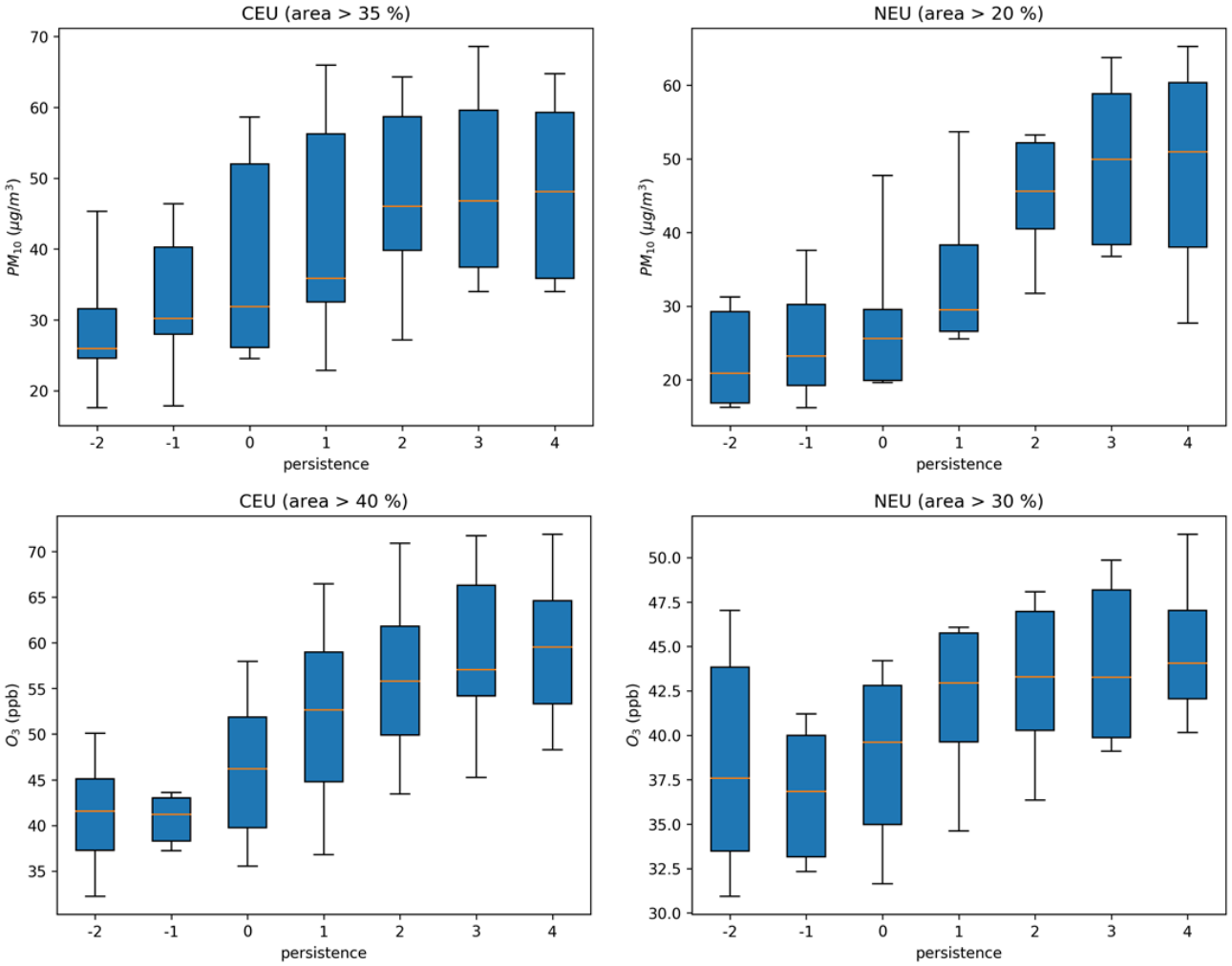

Figure 9: Average evolution of air pollutant concentrations during the most widespread stagnation events over CEU (left) and NEU (right). Results are separately shown for daily background PM_{10} (top) and MDA8 O_3 (bottom) during the 10 stagnation events with the largest area coverage in winter 2002-2011 and summer 1998-2012, respectively. The ticks on the x-axes represent the last two days before the event (-2, -1), the first day of the event (0) and the four following days (1, 2, 3, 4). The boxes extend from the lower (Q1) to the upper (Q3) quartile values of the data, with a horizontal line indicating the position of the median concentrations. The whiskers extend from the boxes to show the range of the data between the 10^{th} and 90^{th} percentiles.

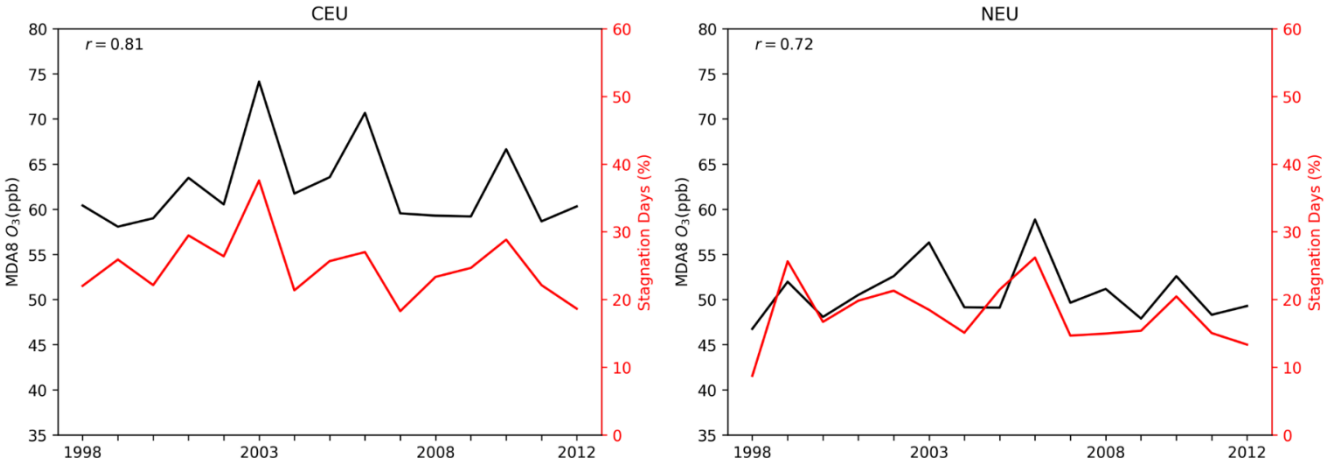

783

784 **Figure 10: Summer time series (1998-2012) of the 95th percentiles of detrended MDA8 O_3 (ppb, black line and left**

785 **y-axis) and the detrended frequency of stagnation days (%, red line and right y-axis) for CEU (left) and NEU (right).**

786 **The upper left corner of each panel shows the correlation coefficient R between both series.**

787

Table 1: Component whose occurrence of stagnant conditions yields the highest R (in brackets) with the frequency of air stagnation days in each region. W_{10}: near-surface wind stagnation; W_{500}: upper wind stagnation; DD: dry days.

Region/Period	Spring	Summer	Autumn	Winter	Year
SCAN	W_{10} (0.86)	W_{10} (0.66)	DD (0.85)	W_{10} (0.88)	W_{10}/W_{500} (0.80)
NEU	DD (0.75)	DD (0.78)	W_{10} (0.85)	W_{10} (0.90)	DD (0.77)
CEU	DD (0.84)	W_{500} (0.81)	W_{500} (0.88)	DD/W_{500} (0.83)	DD (0.83)
SW	W_{500} (0.91)	W_{500} (0.94)	W_{500} (0.93)	W_{500} (0.96)	W_{500} (0.93)
SE	W_{500} (0.70)	W_{500}/DD (0.53)	W_{500} (0.90)	DD (0.75)	W_{500} (0.70)

Table 2: Seasonal and yearly trends in the frequency of air stagnation (days decade^{-1}) for each region during 1979-2016. Significant trends at the 90% confidence level (t-test) are highlighted in bold.

Region	Spring	Summer	Autumn	Winter	Annual
SCAN	-0.53	0.05	**1.44**	-0.31	0.18
NEU	0.49	-0.10	**1.21**	-0.15	**1.48**
CEU	**1.28**	0.43	0.51	-0.37	2.38
SW	0.32	0.02	-0.95	-0.66	-0.46
SE	-0.26	**1.71**	-0.09	-0.27	1.37

Table 3. Trends in the annual occurrence (days decade^{-1}) of near-surface wind stagnation (W_{10}), upper wind stagnation (W_{500}) and dry days (DD) for each region during the period 1979–2016. Significant trends at the 90% confidence level (t-test) are highlighted in bold.

	SCAN	NEU	CEU	SW	SE
W_{10}	0.08	**3.39**	**2.23**	**-2.23**	-0.33
W_{500}	2.52	2.08	3.34	-0.12	**4.82**
DD	-2.52	0.88	**3.30**	0.90	-2.23

Table 4: Average concentration anomalies for winter PM_{10} and summer O_3 in each region, defined as the difference in the seasonal concentrations considering days with and without air stagnation. Absolute anomalies are reported in µg m^{-3} for PM_{10} and ppb for O_3. Relative anomalies (%) have been calculated as the ratio between the absolute anomalies and the seasonal means. The numbers in parentheses represent the number of background stations / grid cells considered for PM_{10} /O_3. No PM_{10} results are reported for SCAN due to the lack of observations in that region.

		SCAN	NEU	CEU	SW	SE
Winter	Absolute (µg m^{-3})	-- (0)	16.3 (88)	16.0 (232)	10.3 (9)	16.1 (11)
PM_{10}	Relative	--	58 %	56 %	45 %	31 %
Summer	Absolute (ppb)	1.5 (149)	6.1 (177)	10.3 (132)	6.0 (103)	6.9 (100)
O_3	Relative	5 %	16 %	23 %	13 %	14 %

Table 5: Characteristic features of air stagnation for each cluster in winter (DJF) / summer (JJA).

Clusters	Interannual Variability	Dominant variable	Synoptic Pattern	Winter PM_{10} / summer O_3
SCAN	** / *	W_{10} / W_{10}	L / H	No data / =
NEU	* / **	W_{10} / DD	L / H	+++ / +
CEU	** / **	DD & W_{500} / W_{500}	H / H	+++ / ++
SW	*** / ****	W_{500} / W_{500}	H / U	+++ / +
SE	** / ***	DD / W_{500} & DD	H / H	+++ / +

The names of the clusters, as displayed on Figure 3, are given in the first column. The second column summarizes the interannual variability, according to the seasonal cycles from Figure 4: * indicates that the seasonal averages of the monthly standard deviation for the number of stagnation days are lower than 1 day, ** between 1 and 1.5 days, * between 1.5 and 2, and **** higher than 2 days. Column 3 indicates the meteorological component from the ASI which better explains the interannual variability of the number of stagnant days within the region, according to Table 1. Column 4 summarizes the synoptic patterns associated with the 5 winters/summers with maximum stagnation, following Figure 5: H (high, positive Z500 anomalies in the region); L (low, negative Z500 anomalies south of the region), and U (undetermined). The last column indicates the impact on the winter PM_{10} / summer O_3 concentrations (following Table 4): = for concentration anomalies under 10 %; + between 10 and 20 %; ++ between 20 and 30%; +++ over 30 %.**